Green Chemical Engineering 1 (2020) 131–139

Contents lists available at ScienceDirect

Green Chemical Engineering

journal homepage: www.keaipublishing.com/en/journals/green-chemical-engineering

Mechanism investigation and catalyst screening of high-temperature reverse water gas shift reaction

Yanying Qi [a], Yi-An Zhu [b], De Chen [a,*]

[a] Norwegian University of Science and Technology, Sem Sælands Veg 4, Trondheim, 7049, Norway
[b] United Chemical Reaction Engineering Research Institute (UNILAB), State Key Laboratory of Chemical Engineering, East China University of Science and Technology, Shanghai, 200237, China

HIGHLIGHTS

- Reaction mechanism of reverse water gas shift (RWGS) reaction on eight metals.
- Microkinetic modeling and degree of rate control analysis of RWGS.
- The two-dimensional volcano plots were constructed to search for new catalysts.
- Several potential bimetallic catalysts were proposed, such as Cu_3Ni.

GRAPHICAL ABSTRACT

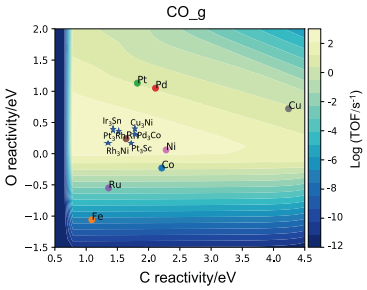

ARTICLE INFO

Keywords:
Reverse water gas shift
Microkinetic modeling
Catalyst screening
Scaling relationship

ABSTRACT

Reverse water gas shift (RWGS) catalysis, a prominent technology for converting CO_2 to CO, is emerging to meet the growing demand of global environment. However, the fundamental understanding of the reaction mechanism is hindered by the complex nature of the reaction. Herein, microkinetic modeling of RWGS on different metals (i.e., Co, Ru, Fe, Ni, Cu, Rh, Pd, and Pt) was performed based on the DFT results to provide the mechanistic insights and achieve the catalyst screening. Adsorption energies of the carbon-based species and the oxygen-based species can be correlated to the adsorption energy of carbon and oxygen, respectively. Moreover, oxygen adsorption energy is an excellent descriptor for the barrier of CO_2 and CO direct dissociation and the difference in reaction barrier between CO_2 (or CO) dissociation and hydrogenation. The reaction mechanism varies on various metals. Direct CO_2 dissociation is the dominating route on Co, Fe, Ru, Rh, Cu, and Ni, while it competes with the COOH-mediated path on Pt and Pd surface. The eights metals can be divided into two groups based on the degree of rate control analysis for CO production, where CO–O bond cleavage is rate relevant on Pt, Pd, and Cu, and OH–H binding is rate-controlling on Co, Fe, Ru, Ni, and Rh. Both CO-direct dissociation and hydrogen-assisted route to CH_4 contribute to the methane formation on Co, Fe, Pt, Pd, Ru, and Rh, despite the significant barrier difference between the two routes. Besides, the specific rate-relevant transition states and intermediates are suggested for methane formation, and thus, the selectivity can be tuned by adjusting the energy. The descriptor (C- and O- formation energy) based microkinetic modeling proposed that the activity trend is Rh∼Ni > Pt∼Pd > Cu > Co > Ru > Fe, where Fe, Co, Ru, and Ni tends to be oxidized. The predicted activity trend is well consistent with those obtained experimentally. The interpolation concept of adsorption energy was used to identify bimetallic materials for highly active catalysts for RWGS.

* Corresponding author.
E-mail address: de.chen@ntnu.no (D. Chen).

https://doi.org/10.1016/j.gce.2020.10.001

Available online 20 November 2020

1. Introduction

Steadily rising CO_2 emission produced by human activities results in negative environmental consequences such as global warming and the increase of global mean sea level. It is imperative to reduce the emission of CO_2. Various carbon capture and storage technologies have been developed for the reduction of CO_2 emission and are employed to capture CO_2 from abundant industrial sources such as fossil fuel-fired power plants. However, the availability of sufficient storage capacity is still an open question. Researchers have devoted efforts to developing more efficient approaches, which could employ CO_2 to produce fuels, chemicals, and hydrocarbons [1–3]. The reverse water-gas shift (RWGS) reaction [4–7] has attracted increasing attention, especially high-temperature RWGS, which offers further CO-based process to methanol as well as long-chain hydrocarbons via Fischer-Tropsch synthesis.

Various metals, including Cu, Fe, Ni, Pd, Pt, Rh, and Au, are active for the RWGS reaction. It is reported that Pd, Ni, and Cu show high catalytic activity with formate groups as an intermediate by combined in-situ FT-IR experiments and first principles [7]. Dai et al. reported that CO_2 RWGS reaction catalytic activities decrease in the order $Ni/CeO_2 > Cu/CeO_2 > Co/CeO_2 > Fe/CeO_2$ [8]. Konsolakis et al. found that CO_2 conversion followed the order: $Co/CeO_2 > Cu/CeO_2 > CeO_2$ [9]. The activity can be affected by reaction condition, catalyst dispersion, particle size, surface morphology, and the nature of the oxide support [2,5,10–12], and thus there is no consensus on the activity trend of various metals. Catalysts screening of RWGS reaction under the consistent criterion is highly desired.

Identify the reaction mechanism is essential to develop a more active and selective catalyst; thus, substantial efforts have been devoted to the mechanism investigation. Different reaction mechanisms have been proposed [12–15], for example, direct CO_2 dissociation, COOH- and HCOO-mediated mechanism. The reaction mechanism depends on the specific catalyst and the reaction condition. DFT calculation found that direct CO_2 dissociation is favorable on Rh, Ni, and Cu, while the COOH-mediated route is preferred on Pt and Pd [16]. The direct dissociate barriers can correlate to the oxygen adsorption strength, where the stronger adsorption of O provides a low CO_2 dissociation barrier and results in the direct dissociation as a favorable route. CO_2 dissociation can be followed by CO methanation reaction. Methane reaction is thermodynamically favored at low temperature, and high pressure [5], especially on Ru, Fe, Ni, Co, and Mo based catalyst [10]. CO methanation can either by CO-direct dissociation route or H-assisted route via HCO or COH, and it is generally accepted that the H-assisted path is more energetic favorable [17–19]. However, the results were mainly based on the analysis of DFT calculations performed at 0 K and 0 bar. It is essential to carry out a microkinetic analysis using temperature and pressure corrected free energy to identify the reaction mechanism and the rate-control steps at the realistic reaction.

Microkinetic modeling based on DFT calculations is a powerful technology for the development of new or improved catalysts without intensive empirical testing. The models enable the incorporation of the fundamental catalytic surface chemistry into a kinetic model, and they can provide a fundamental understanding of reaction mechanism in addition to the prediction of activity and selectivity. Moreover, descriptor-based microkinetic modeling can correlate the activity to two simple descriptors and thus accelerate the catalyst screening. Herein, DFT calculations serve a tool to gain the adsorption energies and activation energies for the catalytic surface reaction among eight metals including Co (0001), Ru (0001), Fe (110), Ni (111), Cu (111), Rh (111), Pd (111) and Pt (111) surfaces. Microkinetic modeling of the RWGS reaction on each surface was carried out to identify the reaction pathway and rate-relevant steps. Descriptor-based microkinetic modeling on the eight metals was performed to predict the activity trend among various metals and achieve further catalyst screening, which could substantially contribute to the discovery of the RWGS catalysts.

2. Methods

2.1. DFT method

All DFT calculations were performed with the Vienna *ab initio* simulation package [20–22], where spin polarisation was employed for Fe, Ni and Co. The exchange-correlation functional was described by using Bayesian error estimation functional with van der Waals correlation (BEEF-vdW) [23]. The interaction between ion cores and valence electrons was described by the projected augmented wave (PAW) method [24], combined with the plane-wave expansion at a kinetic energy cut-off of 400 eV. M (111), M (110), and M (0001) surfaces were modeled by a p (3×3) unit cell with five layers, and a vacuum of 12 Å is set between two periodic repeated slabs. The bottom two layers were fixed at their corresponding bulk positions during the optimization. A $5 \times 5 \times 1$ k-point grid was used to describe the Brillouin zone. The transition state was located by Dimer method [25], and the vibrational frequencies were calculated to confirm the transition states with one negative mode corresponds to the desired reaction coordinates.

The adsorption energy and activation energy were calculated as $E_{ads} = E_{A+slab} - E_A - E_{slab}$ and $E_a = E_{TS} - E_{IS}$, respectively, where E_A is the total energy of the gas phase species, E_{slab} is the total energy of the slab, E_{A+slab} is the minimum total energy of molecule adsorbed on the slab. E_{TS} is the total energy of the transition state, and E_{IS} is the total energy of the initial state.

The Gibbs free energy of each specie is calculated by using the following equation. $G = E + E_{ZPE} + \Delta H^o(0 \rightarrow T) - TS$, where E refers to electric energy determined by DFT, E_{ZPE} is zero-point energy. H, S, and T are enthalpy, entropy, and temperature, respectively. The precise calculation methods for zero-point energy, entropy, and enthalpy of adsorbed species was based on the harmonic approximation, which has been reported in the literature [26,27]. The same vibrational frequencies are employed for all the metals based on the results from Pt (111) since the variations in zero-point energies for various metal surfaces are significantly smaller compared with the adsorption energies [28]. The Gibbs free energies of the gaseous species were calculated with the Shomate equation, where the corresponding Shomate constants were reported in the NIST WebBook [29].

2.2. Microkinetic modeling method

The microkinetic modeling was carried out in Catalysis Microkinetic Analysis Package (CATMAP) [30], which can generate the catalytic trend based on the descriptor-based microkinetic modeling and is suitable for catalysts screening [31,32]. Formation energies are inputs to the model, which were calculated with the total energies of gas-phase CH_4, H_2O, and H_2 as references. The simulation is conducted at $T = 973$ K and $P = 1$ atm with a H_2/CO_2 ratio of 3. High temperature chemical reactions have attracted growing attention for the next-generation energy conversion and storage processes [7]. RWGS reaction is thermodynamically favored by higher temperatures. Besides, the carbon formation by Boudouard reaction and methanation are disfavored at high temperatures. A H_2/CO_2 ratio of 3 was selected for stoichiometrically conversion CO_2 to synthesis gas with a H_2/CO ratio of 2, a typical ratio for methanol synthesis and Fischer-Tropsch synthesis. The reaction rates are generated by solving a mean-field model under the steady-state approximation. The differential equations in the microkinetic models are the following.

$$r_i = k_i^+ \prod_j \theta_{ij} \prod_j P_{ij} - k_i^- \prod_l \theta_{il} \prod_l P_{il}$$

$$\frac{\partial \theta_i s}{\partial t} = \sum s_{ij} r_j$$

where r_i is the rate of each elementary step, k_i^+ and k_i^- are the forward and reverse rate constant, respectively. θ_{ij} and θ_{il} are the site coverage of

surface reactants and products, respectively, while P_{ij} and P_{il} are the pressure of reactants and products, respectively. s_{ij} is stoichiometry coefficients of species i in the elementary step j. $\frac{\partial \theta_i}{\partial t}$ equals zero at the steady-state, and the sum of site converges is constrained to 1. The pre-exponential factors of all the adsorption steps were calculated by assuming the sticking coefficient equals 1 [33].

Three different reaction mechanisms were reported [16], namely, direct CO_2 dissociation mechanism, COOH-mediated mechanism, and the HCOO-mediated mechanism. However, the high stability of HCOO on the surface makes it a spectator rather than a reactive intermediate [34, 35] and results in high barriers for the decomposition of HCOO [36]. Therefore, we considered two reaction pathways, that is direct dissociation and COOH-mediated reaction mechanism, as shown in Scheme 1. Methanation reaction occurs in addition to RWGS reaction, and a better catalyst should own higher RWGS activity and lower methanation activity. Thus, two methane formation pathways are taken into account, that is, CO direct dissociation and H-assisted CO to HCO and HCOH followed by dissociation to CH.

3. Results and discussion

3.1. Adsorption energies of different species

The adsorption energies of various surface species on the eight metal surfaces (i.e., Co (0001), Ru (0001), Fe (110), Ni (111), Cu (111), Rh (111), Pd (111) and Pt (111) surfaces) are summarized in Table 1. The adsorption configurations on Co(0001) have been reported in our previous publications [17,32]. C and O are firmly bound to the surfaces, indicating the high potential of carbonization and oxidation of the metals if it is not consumed efficiently in the reactions. Oxygen prefers to stick on Co (0001), Fe (110), Ru (0001), Ni (111) surfaces, while carbon more strongly binds to Fe (110), Ru (0001), Pt (111), and Rh (111). CO_2, CH_4, and H_2O weakly adsorbed on the surfaces. Most metal surfaces display affinity to CO molecule with adsorption energies from −1.48 eV to −1.82 eV, except for Cu. The adsorption energy of CO on Cu is much lower than others, indicating that CO is more easily desorb from the copper surface rather than participates in the following methanation reactions, which may result in a high CO selectivity.

The adsorption behavior of all the surface species among different metals can be roughly divided into two groups, namely carbon-based (C, CO, CH, CH_2, CH_3, and COOH) and oxygen-based species (O and OH), as illustrated in Fig. 1. The adsorption energies of C, CH, CH_2, and CH_3 among metal surfaces follow a similar trend, where the adsorption becomes weaker in the sequence of Fe, Ru, Rh, Pt, Pd, Co, Ni, and Cu. The pattern of adsorption energies of CO and COOH slightly deviates from the CH_x species. The adsorption strength of O and OH on different metals follows a similar trend.

Fig. 2 illustrates that the adsorption energies of CH, CH_2, CH_3, CH_4, CO, and COOH are correlated to the adsorption energy of C on the various surface since these carbon-based species bind with the metal surface via carbon. The adsorption energies of OH and H_2O can be correlated to the adsorption energy of O. It indicates the adsorption energies can be represented by two descriptors, such as adsorption energies of C and O [37].

3.2. Activation energies

Table 2 summarizes the forward reaction barriers of elementary steps in the RWGS reactions on the eight metal surfaces (i.e., Co (0001), Ru (0001), Fe (110), Ni (111), Cu (111), Rh (111), Pd (111) and Pt (111) surfaces). Hydrogen gas easily dissociates on the most surfaces except for Cu. CO_2 direct dissociation shows barriers smaller than 1.60 eV, indicating CO_2 tends to dissociate on Co (0001), Ru (0001), Fe (110), Ni (111), Cu (111), and Rh (111), compared to the hydrogenation of CO_2, as illustrated in Fig. 3a. The direct CO_2 dissociation barriers on various metal surfaces can be correlated to the adsorption energy of oxygen, as illustrated in Fig. 4a, which is consistent with the previous report [16]. The difference between CO_2 direct dissociation and CO_2 hydrogenation can also be connected to the oxygen adsorption energy. It indicates the surface with higher oxygen-binding strength tends to direct dissociation rather than hydrogenation. The hydrogenation of CO_2 can activate the CO–O(H) bond and decrease the CO–O(H) bond dissociation barrier on Co (0001), Ni (111), Cu (111), Rh (111), Pd (111), and Pt (111) surfaces compared with the direct dissociation. It is difficult to conclude which is the dominating reaction pathway of CO_2 activation based solely on the comparison of the reaction barriers. Thus, microkinetic modeling is necessary to be carried out to figure out the reaction mechanism.

The barriers of elementary steps in the two CO methanation pathways are compared in Fig. 3b. CO direct dissociation (the green column) exhibits high barriers on all the surfaces, and the barriers are higher than 3 eV for the precious metals Pd, Pt, and Cu. Similarly, CO direct dissociation barriers can be correlated to the oxygen adsorption energy, as displayed in Fig. 4a. CO hydrogenation presents lower barriers compared to the direct CO dissociation. The barrier difference between CO hydrogenation and direct dissociation can also be correlated to the oxygen adsorption energy, as illustrated in Fig. 4b. C–O bond dissociation in HCO needs a lower barrier than the direct CO dissociation, and HCO hydrogenation to HCOH can further decrease the C–O bond cleavage barrier. It seems that hydrogen-assisted CO dissociation to methane is energetically favorable on all the metal surfaces. However, the coverage of surface species also plays an essential role in the determination of reaction rates. Thus, the hypothesis needs further validation by microkinetic modeling.

3.3. Microkinetic modeling of each metal surface

We performed microkinetic modeling of each metal surface to identify the reaction mechanism. The reaction rate of each elementary step is summarized in Table 3. The reaction rate of CO_2 direct dissociation is largely higher than COOH-mediated dissociation on Co, Fe, Ru, Rh, Cu, and Ni, while it is just one order of magnitude higher on Pt and Pd. Therefore, we can deduce that the direct CO_2 dissociation is the dominating route on Co, Fe, Ru, Rh, Cu, and Ni, while the two pathways are competing on Pt and Pd.

As we discussed in the last section, CO direct dissociation seems impossible to occur due to extremely high barriers. Surprisingly, their reaction rate of direct CO dissociation is at the same order of magnitude, or just one order of magnitude smaller than the H-assisted dissociation via HCO on Co, Fe, Pt, Pd, Ru, and Rh. It indicates the two reaction pathways for CO methanation compete to occur on these surfaces.

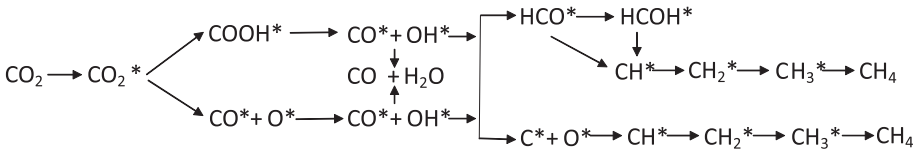

Scheme 1. The elementary steps involved in the microkinetic modeling.

Table 1
Adsorption energies of various surface species on the eight metal surfaces (i.e., Co (0001), Ru (0001), Fe (110), Ni (111), Cu (111), Rh (111), Pd (111) and Pt (111) surfaces).

No.	Species	Co	Fe	Pt	Pd	Ru	Rh	Cu	Ni
1	CO_2	−0.16	−0.65	−0.17	−0.17	−0.37	−0.17	−0.15	−0.16
2	CO	−1.48	−1.71	−1.49	−1.79	−1.75	−1.82	−0.54	−1.66
3	H_2O	−0.30	−0.33	−0.30	−0.29	−0.41	−0.35	−0.21	−0.29
4	OH	−3.48	−4.05	−2.36	−2.47	−3.40	−2.95	−3.05	−3.25
5	O	−5.49	−6.32	−4.13	−4.21	−5.81	−5.02	−4.54	−5.20
6	trans-COOH	−2.22	−2.80	−2.40	−2.15	−2.64	−2.54	−1.59	−2.20
7	CH_4	−0.12	−0.12	−0.14	−0.14	−0.13	−0.13	−0.12	−0.13
8	CH_3	−1.70	−1.89	−2.01	−1.65	−1.89	−1.70	−1.15	−1.60
9	CH_2	−3.54	−4.03	−3.94	−3.53	−4.02	−3.83	−2.64	−3.57
10	CH	−5.64	−6.37	−6.26	−5.77	−6.37	−6.25	−4.23	−5.72
11	C	−6.42	−7.54	−6.81	−6.52	−7.27	−6.99	−4.39	−6.35
12	H	−2.72	−2.93	−2.64	−2.74	−2.81	−2.73	−2.40	−2.72

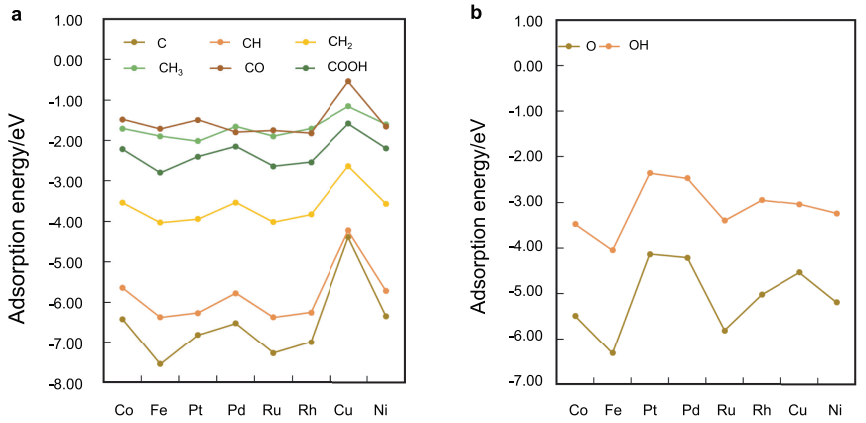

Fig. 1. The adsorption energies of (a) carbon-based species and (b) oxygen-based species among the different metal surfaces Co (0001), Ru (0001), Fe (110), Ni (111), Cu (111), Rh (111), Pd (111) and Pt (111).

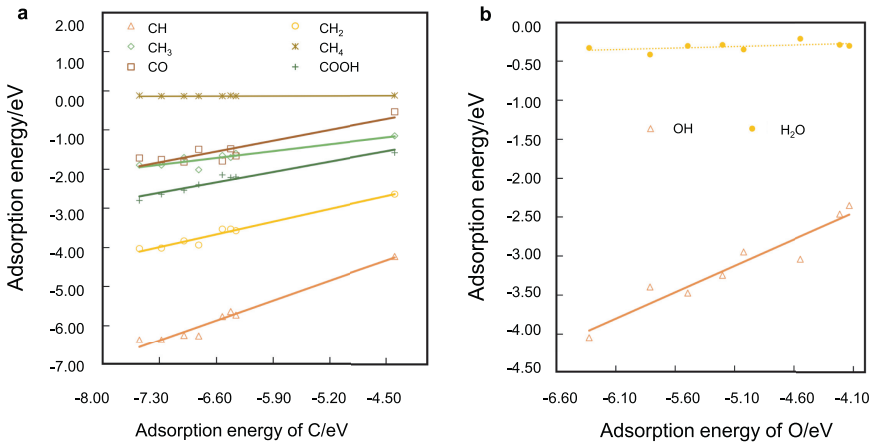

Fig. 2. (a) The adsorption energies of CH, CH_2, CH_3, CH_4, CO, and COOH are correlated to the adsorption energy of C, (b) The adsorption energies of OH and H_2O are correlated to the adsorption energy of O on the various metal surfaces.

Moreover, the HCOH dissociation to CH even owns a lower reaction rate than the direct CO dissociation on Co, Fe, Pt, Pd, Ru, and Rh, despite that the barrier of HCOH to CH is much lower, which may be due to the low coverage of hydrogen. The hydrogen-assisted pathway is the dominating route on Cu and Ni surfaces.

Degree of rate control analysis is a powerful tool to identify the influential transition states, and thus a higher reaction rate can be achieved by adjusting their energies [38,39]. The degree of rate control of each intermediate and transition state to the CO_2 consumption rate and the products (CO and CH_4) generation rate were calculated based on the

Table 2
Forward reaction barriers of elementary steps in the RWGS reactions on the eight metal surfaces (i.e., Co (0001), Ru (0001), Fe (110), Ni (111), Cu (111), Rh (111), Pd (111) and Pt (111) surfaces).

No.	Elementary step	Co	Fe	Pt	Pd	Ru	Rh	Cu	Ni
1	$H_2(g) + 2^* \rightarrow 2H^*$	0.20	−0.05	0.04	0.19	−0.11	−0.08	1.21	0.29
2	$CO_2^* + H^* \rightarrow COOH^* + *$	1.18	1.17	0.64	1.04	1.17	0.87	1.74	1.16
3	$COOH^* + * \rightarrow CO^* + OH^*$	0.30	0.32	0.60	0.60	0.41	0.51	0.26	0.38
4	$CO_2^* + * \rightarrow CO^* + O^*$	0.33	0.00	1.26	1.51	0.28	0.55	1.36	0.66
5	$O^* + H^* \rightarrow OH^* + *$	1.20	1.57	0.84	1.04	1.64	1.25	1.04	1.20
6	$H^* + OH^* \rightarrow H_2O^* + *$	1.47	1.93	0.21	0.70	1.30	0.92	1.23	1.27
7	$CO^* + * \rightarrow C^* + O^*$	2.28	1.27	3.42	3.78	2.06	2.78	3.71	2.82
8	$C^* + H^* \rightarrow CH^* + *$	0.86	0.97	0.70	1.10	1.38	0.83	0.78	0.87
9	$CH^* + H^* \rightarrow CH_2^* + *$	0.54	0.78	0.73	0.93	0.93	0.65	0.63	0.64
10	$CH_2^* + H^* \rightarrow CH_3^* + *$	0.49	0.82	0.57	0.75	0.77	0.47	0.60	0.66
11	$CH_3^* + H^* \rightarrow CH_4(g) + 2^*$	0.90	1.14	0.83	0.66	0.93	0.57	0.73	0.70
12	$CO^* + H^* \rightarrow HCO^* + *$	1.07	0.93	0.94	1.60	1.07	1.28	0.99	1.28
13	$HCO^* + * \rightarrow CH^* + O^*$	0.70	0.49	2.07	2.05	0.85	1.31	1.68	1.05
14	$HCO^* + H^* \rightarrow HCOH^* + *$	1.47	1.79	0.35	1.00	1.23	0.98	0.83	1.18
15	$HCOH^* + * \rightarrow CH^* + OH^*$	0.54	0.17	1.09	1.20	0.35	0.63	1.07	0.68

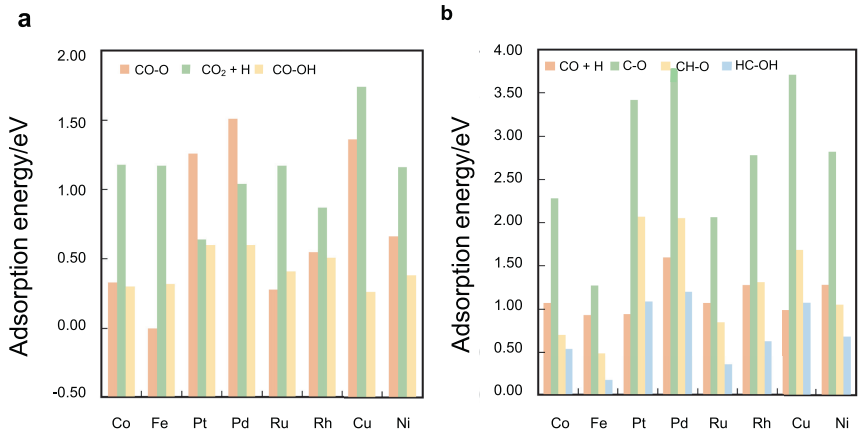

Fig. 3. (a) Forward barriers of CO–O bond cleavage, CO_2 + H bond binding, and CO–OH bond cleavage. (b) Forward barriers of CO + H bond binding, C–O, CH–O and HC-OH bond cleavage on Co (0001), Ru (0001), Fe (110), Ni (111), Cu (111), Rh (111), Pd (111) and Pt (111) surfaces.

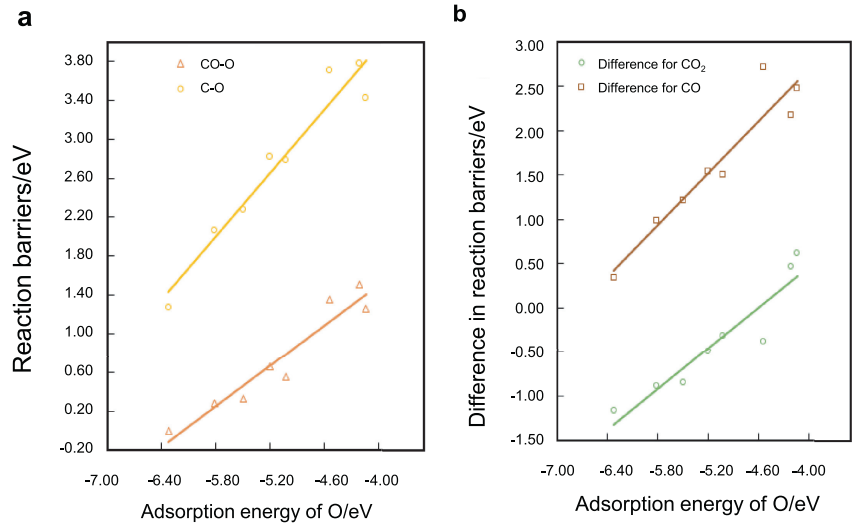

Fig. 4. (a) Reaction barriers of $CO_2^* + * \rightarrow CO^* + O^*$ (labelled as CO–O) and $CO^* + * \rightarrow C^* + O^*$ (labelled as C–O) correlated to the adsorption energy of O. (b) Reaction barrier differences between the direct dissociation and hydrogenation for CO_2 ($CO_2^* + * \rightarrow CO^* + O^*$ and $CO_2^* + H^* \rightarrow COOH^* + *$) and CO ($CO^* + * \rightarrow C^* + O^*$ and $CO^* + H^* \rightarrow HCO^* + *$) correlated to the adsorption energy of O.

Table 3
The reaction rate of elementary steps of RWGS for eight metal surfaces at 973 K and 1 bar with a H_2/CO ratio of 3.

Steps	Co	Fe	Pt	Pd	Ru	Rh	Cu	Ni
$CO_2(g) + * \rightarrow CO_2*$	5.0	9.6×10^{-8}	2.5	1.0×10^{-1}	1.8×10^{-2}	1.5×10^{2}	3.9×10^{-1}	1.1×10^{2}
$H_2(g) + 2* \rightarrow 2H*$	5.0	9.6×10^{-8}	2.5	1.0×10^{-1}	1.8×10^{-2}	1.5×10^{2}	3.9×10^{-1}	1.1×10^{2}
$CO_2* + * \rightarrow CO* + O*$	5.0	9.6×10^{-8}	1.6	7.6×10^{-2}	1.8×10^{-2}	1.5×10^{2}	3.9×10^{-1}	1.1×10^{2}
$CO_2* + H* \rightarrow COOH* + *$	9.1×10^{-5}	2.4×10^{-11}	9.5×10^{-1}	2.9×10^{-2}	1.1×10^{-6}	1.3×10^{-1}	1.3×10^{-7}	2.5×10^{-3}
$COOH* + * \rightarrow CO* + OH*$	9.1×10^{-5}	2.4×10^{-11}	9.5×10^{-1}	2.9×10^{-2}	1.1×10^{-6}	1.3×10^{-1}	1.3×10^{-7}	2.5×10^{-3}
$O* + H* \rightarrow OH* + *$	5.0	9.6×10^{-8}	1.6	7.6×10^{-2}	1.8×10^{-2}	1.5×10^{2}	3.9×10^{-1}	1.1×10^{2}
$H* + OH* \rightarrow H_2O* + *$	5.0	9.6×10^{-8}	2.5	1.0×10^{-1}	1.8×10^{-2}	1.5×10^{2}	3.9×10^{-1}	1.1×10^{2}
$H_2O* + * \rightarrow H_2O(g) + 2*$	5.0	9.6×10^{-8}	2.5	1.0×10^{-1}	1.8×10^{-2}	1.5×10^{2}	3.9×10^{-1}	1.1×10^{2}
$CO* \rightarrow CO(g) + *$	5.0	9.6×10^{-8}	2.5	1.0×10^{-1}	1.8×10^{-2}	1.5×10^{2}	3.9×10^{-1}	1.1×10^{2}
$CO* + * \rightarrow C* + O*$	6.2×10^{-16}	3.5×10^{-29}	1.8×10^{-18}	6.1×10^{-21}	5.3×10^{-19}	1.3×10^{-12}	8.2×10^{-21}	9.1×10^{-15}
$CO* + H* \rightarrow HCO*$	9.4×10^{-15}	1.3×10^{-28}	1.7×10^{-14}	6.1×10^{-19}	5.8×10^{-19}	9.6×10^{-12}	3.5×10^{-17}	2.4×10^{-13}
$HCO* + * \rightarrow CH* + O*$	9.4×10^{-15}	1.3×10^{-28}	6.3×10^{-17}	7.0×10^{-20}	5.8×10^{-19}	7.7×10^{-12}	3.3×10^{-17}	2.4×10^{-13}
$HCO* + H* \rightarrow HCOH* + *$	1.9×10^{-20}	2.6×10^{-33}	1.7×10^{-14}	5.4×10^{-19}	1.1×10^{-21}	1.9×10^{-12}	2.1×10^{-18}	4.5×10^{-16}
$HCOH* + * \rightarrow CH* + OH*$	1.9×10^{-20}	2.6×10^{-33}	1.7×10^{-14}	5.4×10^{-19}	1.1×10^{-21}	1.9×10^{-12}	2.1×10^{-18}	4.5×10^{-16}
$C* + H* \rightarrow CH* + *$	6.2×10^{-16}	3.5×10^{-29}	1.8×10^{-18}	6.1×10^{-21}	5.3×10^{-19}	1.3×10^{-12}	8.2×10^{-21}	9.1×10^{-15}
$CH* + H* \rightarrow CH_2* + *$	1.0×10^{-14}	1.7×10^{-28}	1.7×10^{-14}	6.1×10^{-19}	1.1×10^{-18}	1.1×10^{-11}	3.5×10^{-17}	2.5×10^{-13}
$CH_2* + H* \rightarrow CH_3* + *$	1.0×10^{-14}	1.7×10^{-28}	1.7×10^{-14}	6.1×10^{-19}	1.1×10^{-18}	1.1×10^{-11}	3.5×10^{-17}	2.5×10^{-13}
$CH_3* + H* \rightarrow CH_4(g) + 2*$	1.0×10^{-14}	1.7×10^{-28}	1.7×10^{-14}	6.1×10^{-19}	1.1×10^{-18}	1.1×10^{-11}	3.5×10^{-17}	2.5×10^{-13}

following equation. X_{ij} is the degree of rate control matrix, r_i is the rate of production for product i, G_j is the free energy of species j, k is Boltzmann's constant, and T is the temperature.

$$X_{ij} = \frac{dlog(r_i)}{d(-G_j/kT)}$$

We summarized the most influential transition states and intermediates in Table 4. The same rate-determining steps are observed for the CO_2 conversation rate and CO production rate. It is elucidated that H–OH or CO–O is the rate-determining transition state, despite that the exact value varies on various metals. The eights metals can be divided into two groups based on the rate-determining step. CO–O bond cleavage is rate-determining on Pt, Pd, and Cu, owing to the high barrier on the surfaces, while OH binding with H to H_2O is rate-determining on Co, Fe, Ru, Ni, and Rh. A negative degree of rate control of CO_2 binding energy is found on Co, Fe, and Ru, while O on Ru and Ni. The negative value indicates that decrease the adsorption stability of the surface species could increase the activity.

Additional rate-determining states or intermediates can affect the methane formation rate, in addition to the same rate-determining step with CO_2 consumption rate. CO desorption has a negative effect on the methane formation on Co, Pt, and Cu, while O on Co, and Fe. CH_3–H bond cleavage is the rate-relevant one for Co, Fe, and Ru, which is attributed to the higher barrier of the step. HC-OH bond cleavage is rate-controlling for Pt and Pd, HC-O for Rh and Cu, and CH_2–H for Ni. These specific rate-relevant steps for methane is also the rate-controlling steps for methane selectivity. Tuning the energies for the particular rate-relevant transition states and intermediates can modify methane selectivity.

3.4. Descriptor based microkinetic modeling of all metals

The descriptor-based microkinetic modeling is a versatile tool to predict the catalyst activity trend and achieve catalyst screening. As we discussed, the adsorption energies of different surface species can be correlated to the carbon or oxygen binding energy. Thus, we employed the formation energy of C* and O* as two descriptors to describe the reaction kinetics of RWGS. Brønsted-Evans-Polanyi [40,41] relations were employed for transition-state scaling relations of all the steps except CO_2 and CO dissociation. CO_2 and CO dissociation are correlated to the final state in our setting since the barrier can be connected to the oxygen binding energy, as we discussed above.

O and H are the abundant surface species at the reaction condition 973 K, as displayed in Fig. 5. Talin et al. reported that the most abundant surface species are CO and H at 500 K [13]. The contrary is due to the modelings were performed at different temperatures. CO desorption becomes much easier compared to the CO dissociation or hydrogenation at high temperatures. Fe, Co, Ru, and Ni are covered by oxygen, indicating these surfaces are oxidized at this reaction condition, which is attributed to the strong bonding between oxygen and metal and the high barrier of oxygen hydrogenation on these surfaces.

The activity of CO formation is in the sequence of Rh∼Ni > Pt∼Pd> Cu > Co > Ru > Fe, which is consistent with the experimental result from Dai et al. [8]. They reported that RWGS reaction catalytic activities are ranked as follows: Ni–CeO_2 > Cu–CeO_2 > Co–C eO_2 > Fe–CeO_2. The turnover frequency of methane formation is many orders of magnitude smaller than CO formation, and the activity trend of CH_4 formation is in the sequence of Rh∼Ni > Pt∼Pd∼Co > Cu > Ru > Fe.

We can find that CO selectivity is almost 100% for all the metals at high temperatures, which agrees with the experimental result performed at high temperatures [7]. They reported that CO selectivity of Pd and Cu achieve 100% CO selectivity at 973 K with $H_2/CO = 3$, while it is slightly lower than 100% on Ni. Increasing the temperature or decreasing the H_2/CO ratio can achieve 100% CO selectivity on Ni. Moreover, we calculated the ratio between the CO formation rate and methane formation rate (CO/CH_4) and plotted the descriptor-based ratio mapping. CO/CH_4 ratio selectivity ranks as follows: Cu∼Fe > Ru∼Pt∼Pd >

Table 4
Degree of rate control analysis for the CO_2 consumption rate as well as CO and CH_4 production rate.

	Co	Fe	Pt	Pd	Ru	Rh	Cu	Ni
CO_2 and CO	H–OH: 1.84 CO_2: -0.78	H–OH: 1.98 CO_2: -1.02	CO–O: 0.62	CO–O: 0.72	H–OH: 1.99 CO_2: -1 O: -2	H–OH: 0.02	CO–O: 1.00	H–OH: 0.25 O: -0.23
CH_4	CH_3–H: 0.97 H–OH: 3.97 CO_2: -2.82 CO: 0.89 O: -2.68	H–OH: 3.94 CH_3–H: 0.95 CO_2: -3.05 O: -3.05	CO–O: 0.62 HC-OH: 0.99 CO: -1.02	CO–O: 0.73 HC-OH: 0.88	CH_3–H: 0.96 H–OH: 4.02 CO_2: -2.98 O: -2.97	CH–O: 0.49 H–OH: 0.30	CO–O: 0.91 HC-O: 0.86 CO: -1	CH_2–H: 0.60 H–OH: 1.38 CO_2: -0.4 O: -0.46

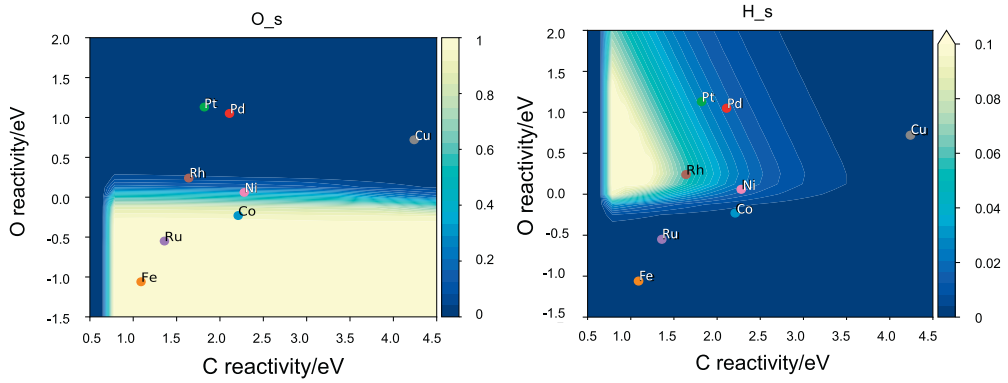

Fig. 5. Site coverages of O and H in RWGS on Co (0001), Ru (0001), Fe (110), Ni (111), Cu (111), Rh (111), Pd (111), and Pt (111) surfaces at 973 K and 1 bar with $H_2/CO = 3$.

Co > Ni > Rh, which is consistent with the experimental results. Chen et al. found that the trend of CO/CH_4 ratio is Pt > Co > Ni. [42].

Fig. 6 demonstrated that the most active catalysts own the carbon formation energy and the oxygen formation energy around 1.64 and 0.24 eV, respectively. The interpolation concept of adsorption energy was used to search for potentially interesting bimetallic catalysts [43,44]. We performed DFT calculations to get the carbon and oxygen formation energies on hundreds of A_3B type bimetal terrace surfaces, where *M* and *N* represent metals. As we found above, the methane selectivity is very low for all the metals. Thus only the energies close to the predicted optimum carbon and oxygen formation energies are interesting to us, as shown in Fig. 7. We identified potential bimetals with high activity, that is, Cu_3Ni, Ir_3Sn, Pd_3Co, Pt_3Co, Pt_3Rh, Pt_3Sc, and Rh_3 (Sc/Ga/Ge/In/Ir/Ni/Zn). PtCo has been reported to be highly active for the RWGS in the literature [42,45]. Cu_3Ni is identified as to allow cost and highly active catalysts, which has recently been demonstrated by Xiao and coworkers [46]. The other catalysts need further experimental validation.

4. Conclusion

The adsorption behavior of all the surface species on different metals can be split into two groups, carbon-based and oxygen-based species. Each group follows a similar trend among metals, which indicates that two descriptors can represent the adsorption energies of various species. It is difficult to identify the dominating route for CO_2 dissociation to CO by solely comparing the reaction barriers. In contrast, hydrogen-assisted CO dissociation to methane is energetically favorable on all the metal surfaces.

The microkinetic modeling suggested that the direct CO_2 dissociation is the favorable pathway on Co, Fe, Ru, Rh, Cu, and Ni, while it competes with the COOH-mediated route on Pt and Pd. CO direct dissociation and

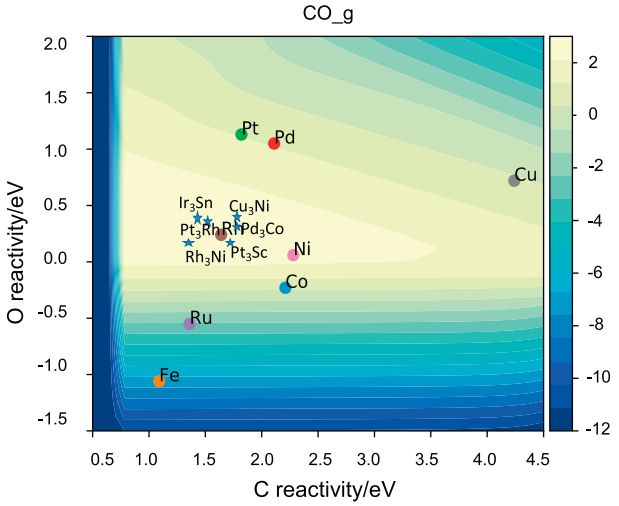

Fig. 7. The potential bimetal catalysts for high-temperature RWGS. It is noted that some potential ones are not labelled here for the sake of clarity.

H-assisted pathways for CO methanation compete to occur on Co, Fe, Pt, Pd, Ru, and Rh, despite that the high barriers of CO direct dissociation. It demonstrates that it is appropriate to identify the reaction mechanism by performing microkinetic modeling rather than exclusively comparing the reaction barrier.

The degree of rate control analysis demonstrates that the rate-determining step varies on different surfaces. CO–O bond cleavage is

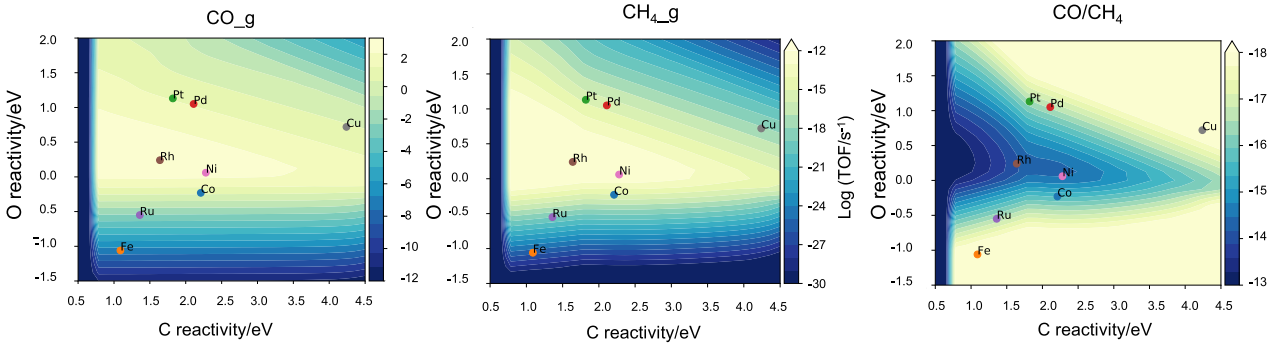

Fig. 6. Predicted activity for CO and CH_4 formation and CO/CH_4 ratio (defined as the ratio between CO formation rate and CH_4 formation rate) in RWGS on Co (0001), Ru (0001), Fe (110), Ni (111), Cu (111), Rh (111), Pd (111) and Pt (111) surfaces at 973 K and 1 bar with $H_2/CO = 3$.

the rate-determining on Pt, Pd, and Cu, while OH binding with H to H_2O is rate-determining on Co, Fe, Ru, Ni, and Rh. Methane formation has an additional rate-controlling step, which is CH_3–H bond cleavage for Co, Fe, and Ru, HC-OH for Pt and Pd, HC-O for Rh and Cu, and CH_2–H for Ni. The methane selectivity can be hindered by adjusting the surface properties to increase the barrier of the rate-determining step for methanation.

Two-dimensional volcano plots were constructed by coupling the scaling relations in a microkinetic model using C- and O- formation energy as descriptors. The microkinetic modeling elucidates that the activity trend of CO formation is in the sequence of Rh∼Ni > Pt∼Pd > Cu > Co > Ru > Fe, which agrees with the reported experimental results. Moreover, the model suggests that Fe, Co, Ru, and Ni tend to be oxidized at the reaction condition. We also constructed volcano plots of the ratio of CO/CH_4 as a function of the two descriptors. The two-dimensional volcano plots were used to search for new alloy catalysts of high activity and low selectivity to methane, based on the interpolation concept of adsorption energy. As a result, several bimetallic catalysts were identified to be potentially interesting catalyst materials, where the Cu_3Ni was screened as a candidate with a low cost and high activity.

Declaration of competing interest

The authors declare that they have no known competing financial interests or personal relationships that could have appeared to influence the work reported in this paper.

Acknowledgments

The financial support from the Centre for Industrial Catalysis Science and Innovation (iCSI), which receives financial support from the NO-237922. The Research Council of Norway, is gratefully acknowledged.

References

[1] G. Centi, S. Perathoner, Opportunities and prospects in the chemical recycling of carbon dioxide to fuels, Catal. Today 148 (2009) 191–205.
[2] S. Kattel, P. Liu, J.G. Chen, Tuning selectivity of CO_2 hydrogenation reactions at the metal/oxide interface, J. Am. Chem. Soc. 139 (2017) 9739–9754.
[3] R.P. Ye, J. Ding, W.B. Gong, M.D. Argyle, Q. Zhong, Y.J. Wang, C.K. Russell, Z.H. Xu, A.G. Russell, Q.H. Li, M.H. Fan, Y.G. Yao, CO_2 hydrogenation to high-value products via heterogeneous catalysis, Nat. Commun. 10 (2019) 15.
[4] C.-S. Chen, W.-H. Cheng, S.-S. Lin, Study of iron-promoted Cu/SiO_2 catalyst on high temperature reverse water gas shift reaction, Appl. Catal. Gen. 257 (2004) 97–106.
[5] F. Vidal Vázquez, P. Pfeifer, J. Lehtonen, P. Piermartini, P. Simell, V. Alopaeus, Catalyst screening and kinetic modeling for CO production by high pressure and temperature reverse water gas shift for Fischer–Tropsch applications, Ind. Eng. Chem. Res. 56 (2017) 13262–13272.
[6] F. Bustamante, R.M. Enick, A.V. Cugini, R.P. Killmeyer, B.H. Howard, K.S. Rothenberger, M.V. Ciocco, B.D. Morreale, S. Chattopadhyay, S. Shi, High-temperature kinetics of the homogeneous reverse water–gas shift reaction, AIChE J. 50 (2004) 1028–1041.
[7] S. Choi, B.-I. Sang, J. Hong, K.J. Yoon, J.-W. Son, J.-H. Lee, B.-K. Kim, H. Kim, Catalytic behavior of metal catalysts in high-temperature RWGS reaction: in-situ FT-IR experiments and first-principles calculations, Sci. Rep. 7 (2017) 41207.
[8] B. Dai, G. Zhou, S. Ge, H. Xie, Z. Jiao, G. Zhang, K. Xiong, CO_2 reverse water-gas shift reaction on mesoporous M-CeO_2 catalysts, Can. J. Chem. Eng. 95 (2017) 634–642.
[9] M. Konsolakis, M. Lykaki, S. Stefa, S.a.C. Carabineiro, G. Varvoutis, E. Papista, G.E. Marnellos, CO_2 hydrogenation over nanoceria-supported transition metal catalysts: role of ceria morphology (nanorods versus nanocubes) and active phase nature (Co versus Cu), Nanomaterials 9 (2019) 1739.
[10] N. Podrojková, V. Sans, A. Oriňak, R. Oriňaková, Recent developments in the modelling of heterogeneous catalysts for CO_2 conversion to chemicals, ChemCatChem 12 (2020) 1802–1825.
[11] M. Zhu, Q. Ge, X. Zhu, Catalytic reduction of CO_2 to CO via reverse water gas shift reaction: recent advances in the design of active and selective supported metal catalysts, Trans. Tianjin Univ. 26 (2020) 172–187.
[12] Y.A. Daza, J.N. Kuhn, CO_2 conversion by reverse water gas shift catalysis: comparison of catalysts, mechanisms and their consequences for CO_2 conversion to liquid fuels, RSC Adv. 6 (2016) 49675–49691.
[13] T. Avanesian, G.S. Gusmão, P. Christopher, Mechanism of CO_2 reduction by H_2 on Ru(0001) and general selectivity descriptors for late-transition metal catalysts, J. Catal. 343 (2016) 86–96.
[14] D. Cheng, F.R. Negreiros, E. Aprà, A. Fortunelli, Computational approaches to the chemical conversion of carbon dioxide, ChemSusChem 6 (2013) 944–965.
[15] M. Maestri, K. Reuter, Molecular-level understanding of WGS and reverse WGS reactions on Rh through hierarchical multiscale approach, Chem. Eng. Sci. 74 (2012) 296–299.
[16] L. Dietz, S. Piccinin, M. Maestri, Mechanistic insights into CO_2 activation via reverse water–gas shift on metal surfaces, J. Phys. Chem. C 119 (2015) 4959–4966.
[17] Y. Qi, J. Yang, X. Duan, Y.-A. Zhu, D. Chen, A. Holmen, Discrimination of the mechanism of CH_4 formation in Fischer–Tropsch synthesis on Co catalysts: a combined approach of DFT, kinetic isotope effects and kinetic analysis, Catal. Sci. Technol. 4 (2014) 3534–3543.
[18] M. Ojeda, R. Nabar, A.U. Nilekar, A. Ishikawa, M. Mavrikakis, E. Iglesia, CO activation pathways and the mechanism of Fischer–Tropsch synthesis, J. Catal. 272 (2010) 287–297.
[19] J.L.C. Fajín, J.R.B. Gomes, M.N.D.S. Cordeiro, Mechanistic study of carbon monoxide methanation over pure and Rhodium- or Ruthenium-doped nickel catalysts, J. Phys. Chem. C 119 (2015) 16537–16551.
[20] G. Kresse, J. Furthmuller, Efficiency of ab-initio total energy calculations for metals and semiconductors using a plane-wave basis set, Comput. Mater. Sci. 6 (1996) 15–50.
[21] G. Kresse, J. Hafner, Ab initio molecular dynamics for liquid metals, Phys. Rev. B 47 (1993) 558–561.
[22] G. Kresse, J. Hafner, Ab initio molecular dynamics for open-shell transition metals, Phys. Rev. B 48 (1993) 13115–13118.
[23] J. Wellendorff, K.T. Lundgaard, A. Mogelhoj, V. Petzold, D.D. Landis, J.K. Norskov, T. Bligaard, K.W. Jacobsen, Density functionals for surface science: Exchange-correlation model development with Bayesian error estimation, Phys. Rev. B 85 (2012) 235149.
[24] G. Kresse, D. Joubert, From ultrasoft pseudopotentials to the projector augmented-wave method, Phys. Rev. B 59 (1999) 1758–1775.
[25] G. Henkelman, H. Jónsson, Improved tangent estimate in the nudged elastic band method for finding minimum energy paths and saddle points, J. Chem. Phys. 113 (2000) 9978–9985.
[26] Y. Qi, C. Aaserud, J. Yang, A. Holmen, D. Chen, Promotional effect of in-situ generated hydroxyl on olefin selectivity of Co-catalyzed Fischer-Tropsch synthesis, Phys. Chem. Chem. Phys. 21 (2019) 24441–24448.
[27] Y.-A. Zhu, D. Chen, X.-G. Zhou, W.-K. Yuan, DFT studies of dry reforming of methane on Ni catalyst, Catal. Today 148 (2009) 260–267.
[28] T. Bligaard, K. Honkala, A. Logadottir, J.K. Nørskov, S. Dahl, C.J.H. Jacobsen, On the compensation effect in heterogeneous catalysis, J. Phys. Chem. B 107 (2003) 9325–9331.
[29] NIST Chemistry WebBook, NIST Standard Reference Database Number 69.
[30] A.J. Medford, C. Shi, M.J. Hoffmann, A.C. Lausche, S.R. Fitzgibbon, T. Bligaard, J.K. Nørskov, CatMAP: a software package for descriptor-based microkinetic mapping of catalytic trends, Catal. Lett. 145 (2015) 794–807.
[31] D. Xu, P. Wu, B. Yang, Essential role of water in the autocatalysis behavior of methanol synthesis from CO_2 hydrogenation on Cu: a combined DFT and microkinetic modeling study, J. Phys. Chem. C 123 (2019) 8959–8966.
[32] Y. Wang, L. Xiao, Y. Qi, M. Mahmoodinia, X. Feng, J. Yang, Y.-A. Zhu, D. Chen, Towards rational catalyst design: boosting the rapid prediction of transition-metal activity by improved scaling relations, Phys. Chem. Chem. Phys. 21 (2019) 19269–19280.
[33] L.C. Grabow, M. Mavrikakis, Mechanism of methanol synthesis on Cu through CO_2 and CO hydrogenation, ACS Catal. 1 (2011) 365–384.
[34] E. Vesselli, M. Rizzi, L. De Rogatis, X. Ding, A. Baraldi, G. Comelli, L. Savio, L. Vattuone, M. Rocca, P. Fornasiero, A. Baldereschi, M. Peressi, Hydrogen-assisted transformation of CO_2 on nickel: the role of formate and carbon monoxide, J. Phys. Chem. Lett. 1 (2010) 402–406.
[35] S. Eckle, H.-G. Anfang, R.J. Behm, Reaction intermediates and side products in the methanation of CO and CO_2 over supported Ru catalysts in H_2-rich reformate gases, J. Phys. Chem. C 115 (2011) 1361–1367.
[36] R.C. Catapan, A.a.M. Oliveira, Y. Chen, D.G. Vlachos, DFT study of the water–gas shift reaction and coke formation on Ni (111) and Ni (211) surfaces, J. Phys. Chem. C 116 (2012) 20281–20291.
[37] F. Abild-Pedersen, J. Greeley, F. Studt, J. Rossmeisl, T.R. Munter, P.G. Moses, E. Skúlason, T. Bligaard, J.K. Nørskov, Scaling properties of adsorption energies for hydrogen-containing molecules on transition-metal surfaces, Phys. Rev. Lett. 99 (2007) 016105.
[38] C.T. Campbell, The degree of rate control: a powerful tool for catalysis research, ACS Catal. 7 (2017) 2770–2779.
[39] C. Stegelmann, A. Andreasen, C.T. Campbell, Degree of rate control: how much the energies of intermediates and transition states control rates, J. Am. Chem. Soc. 131 (2009) 8077–8082.
[40] S. Wang, B. Temel, J. Shen, G. Jones, L.C. Grabow, F. Studt, T. Bligaard, F. Abild-Pedersen, C.H. Christensen, J.K. Nørskov, Universal Brønsted-Evans-Polanyi relations for C–C, C–O, C–N, N–O, N–N, and O–O dissociation reactions, Catal. Lett. 141 (2011) 370–373.
[41] S. Wang, V. Petzold, V. Tripkovic, J. Kleis, J.G. Howalt, E. Skúlason, E.M. Fernández, B. Hvolbæk, G. Jones, A. Toftelund, H. Falsig, M. Björketun, F. Studt, F. Abild-Pedersen, J. Rossmeisl, J.K. Nørskov, T. Bligaard, Universal transition state scaling relations for (de)hydrogenation over transition metals, Phys. Chem. Chem. Phys. 13 (2011) 20760–20765.
[42] M.D. Porosoff, J.G. Chen, Trends in the catalytic reduction of CO_2 by hydrogen over supported monometallic and bimetallic catalysts, J. Catal. 301 (2013) 30–37.

[43] J.S. Yoo, F. Abild-Pedersen, J.K. Nørskov, F. Studt, Theoretical analysis of transition-metal catalysts for formic acid decomposition, ACS Catal. 4 (2014) 1226–1233.
[44] J.K. Nørskov, F. Abild-Pedersen, F. Studt, T. Bligaard, Density functional theory in surface chemistry and catalysis, Proc. Natl. Acad. Sci. Unit. States Am. 108 (2011) 937.
[45] S. Kattel, W. Yu, X. Yang, B. Yan, Y. Huang, W. Wan, P. Liu, J.G. Chen, CO_2 hydrogenation over oxide-supported PtCo catalysts: the role of the oxide support in determining the product selectivity, Angew. Chem., Int. Ed. Engl. 55 (2016) 7968–7973.
[46] L.-X. Wang, E. Guan, Z. Wang, L. Wang, Z. Gong, Y. Cui, Z. Yang, C. Wang, J. Zhang, X. Meng, P. Hu, X.-Q. Gong, B.C. Gates, F.-S. Xiao, Dispersed nickel boosts catalysis by copper in CO_2 hydrogenation, ACS Catal. 10 (2020) 9261–9270.